A Dual-Bioinspired Structural Design Enables Highly Efficient Microwave Absorption and Thermal Insulation in SiC Hybrid Aerogels

Jingwen Deng [a], Huimin Liu [a], Xin Zhang [a], Yi Zhang [a], Bing Liu [a], Liyuan Han [c,*], Hejun Li [a,*], Xuemin Yin [a,b,*]

[a] *Shaanxi Key Laboratory of Fiber Reinforced Light Composite Materials, Carbon/Carbon Composites Research Center, Northwestern Polytechnical University, Xi'an, Shaanxi, 710072, PR China*

[b] *Department of Aeronautical and Aviation Engineering, The Hong Kong Polytechnic University, Hung Hom, Kowloon, Hong Kong, 999077, PR China*

[c] *Henan Key Laboratory of High Performance Carbon Fiber Reinforced Composites, Institute of Carbon Matrix Composites, Henan Academy of Sciences, Zhengzhou, Henan, 450046, PR China*

E-mail for corresponding author:

hanliyuan@hnas.ac.cn (Dr. Liyuan Han)

lihejun@nwpu.edu.cn (Prof. Hejun Li)

yinxuemin@nwpu.edu.cn ; xuemin.yin@polyu.edu.hk (Dr. Xuemin Yin)

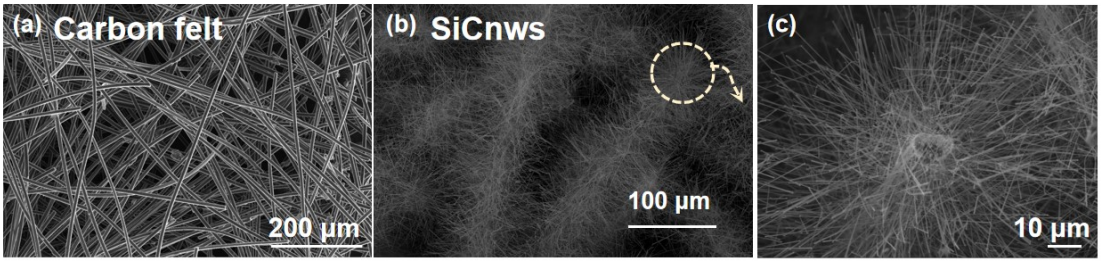

Fig. S1 Low magnification SEM images of carbon felt (a) and SiCnws/C_f (b).

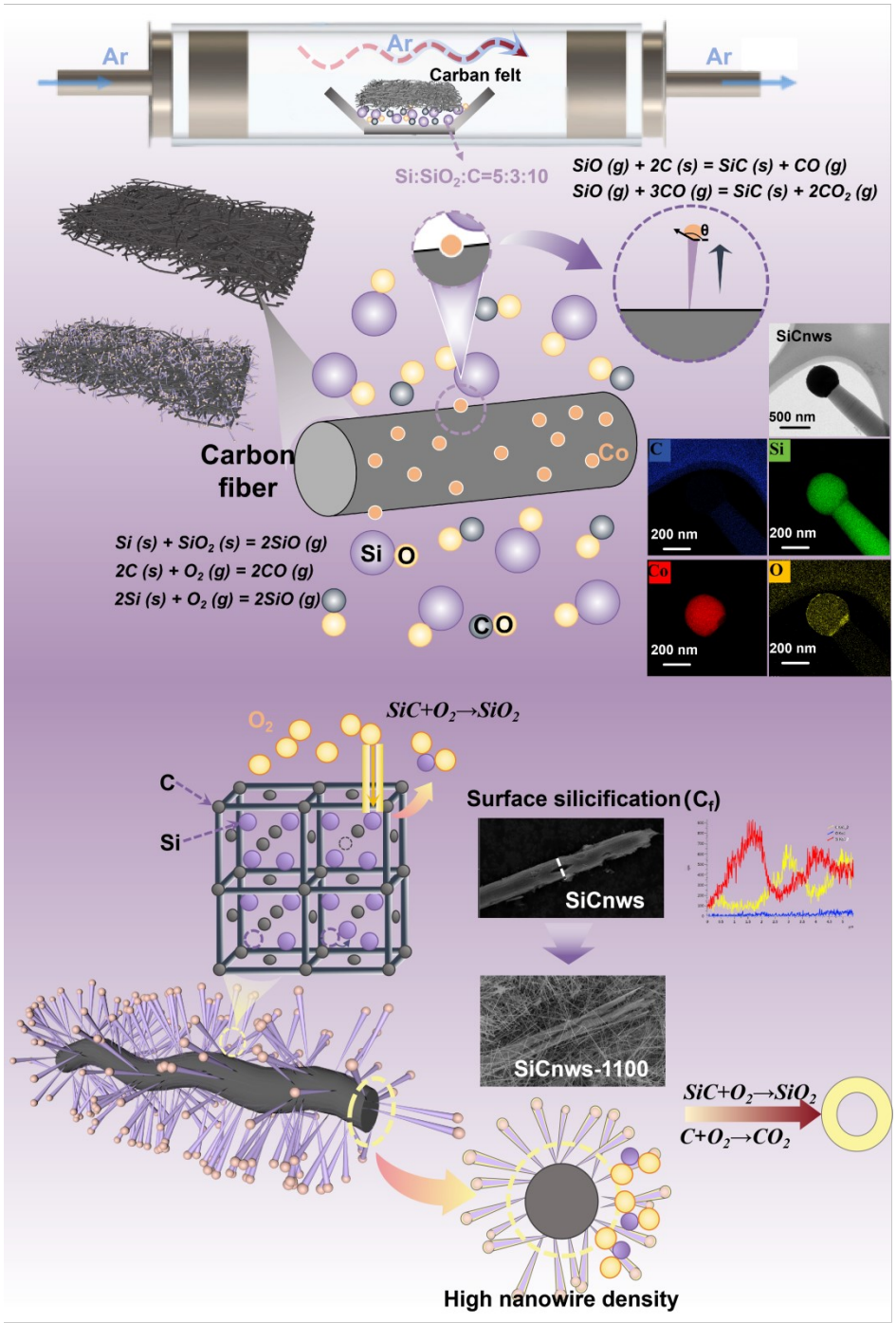

Fig. S2 Growth mechanism of SiC nanowires on carbon felt and hollow microtube.

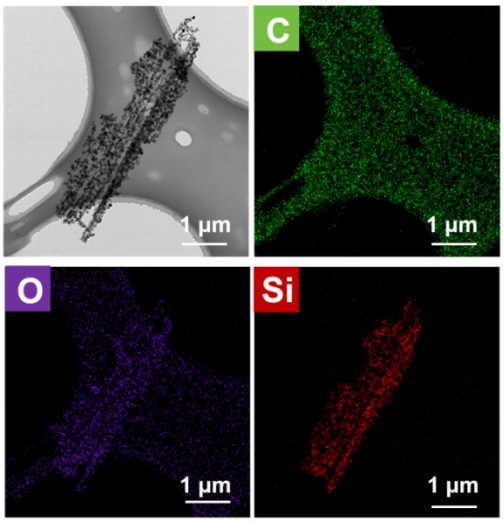

Fig. S3 TEM images and their corresponding EDX mapping images of oxidized skeleton for SiCnws-1100.

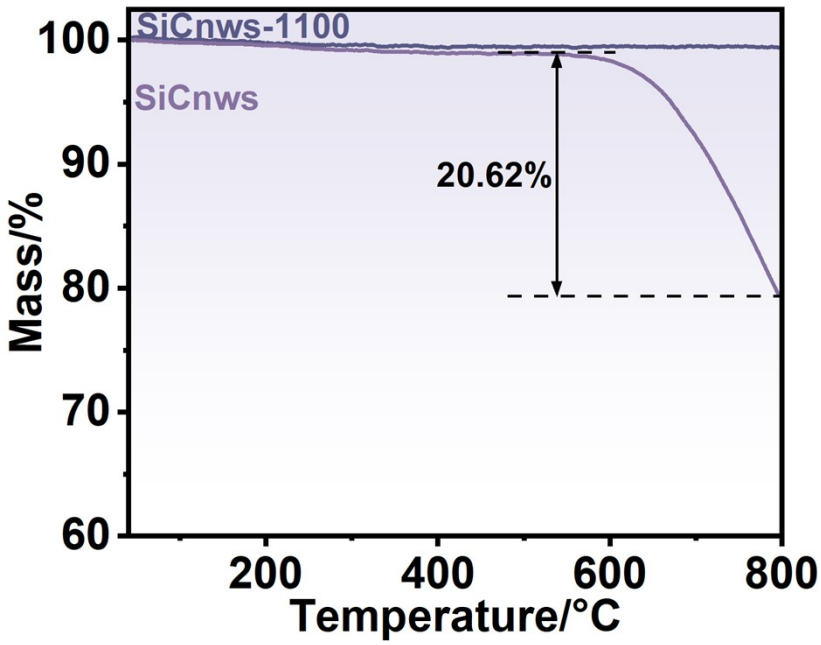

Fig. S4 TG curve of aerogels before and after oxidation.

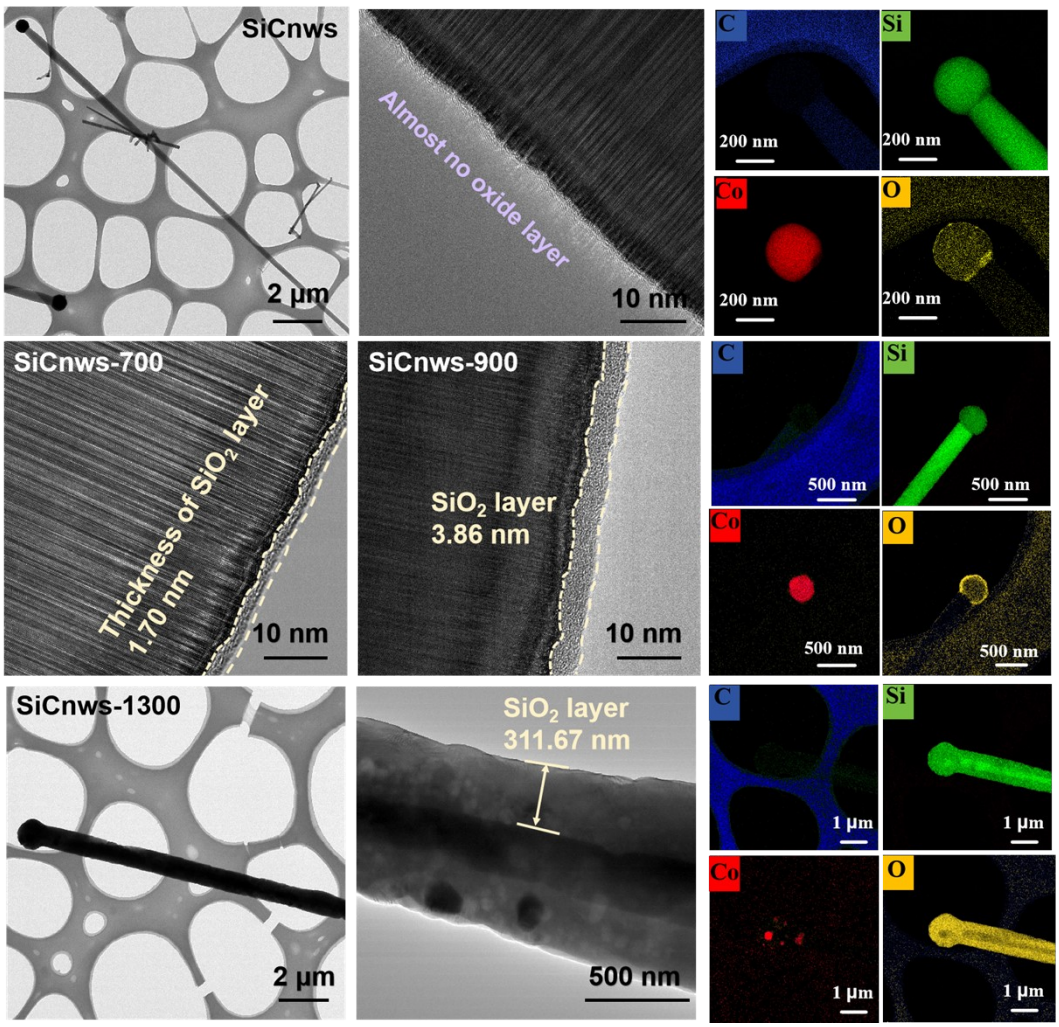

Fig. S5 TEM photographs of SiC aerogels at different oxidation temperatures

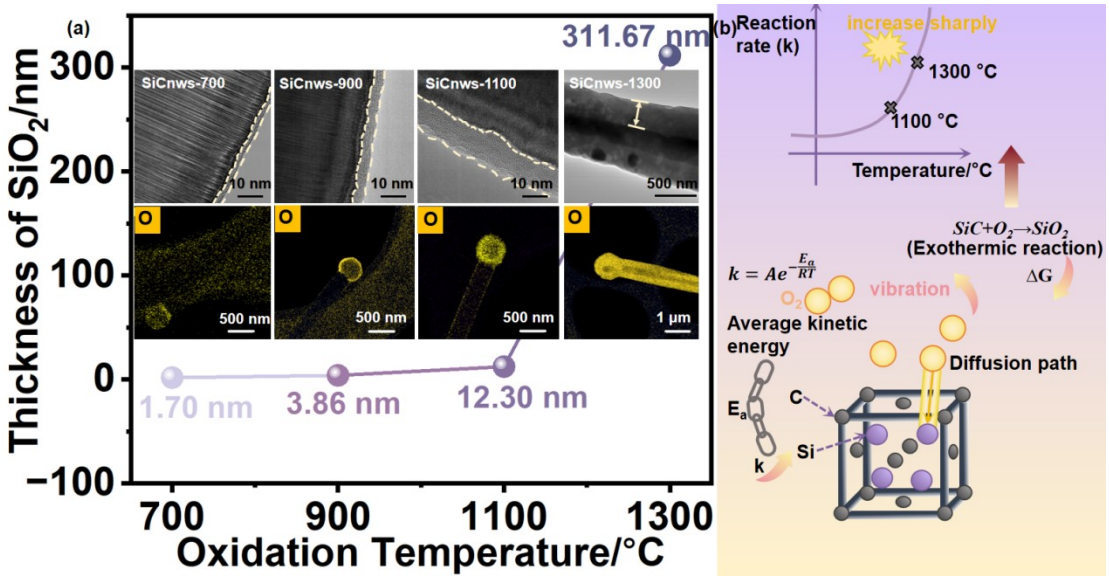

Fig. S6 Diagram of the relationship between oxidation temperature and oxide layer thickness (a), and schematic diagram of the influencing mechanism (b).

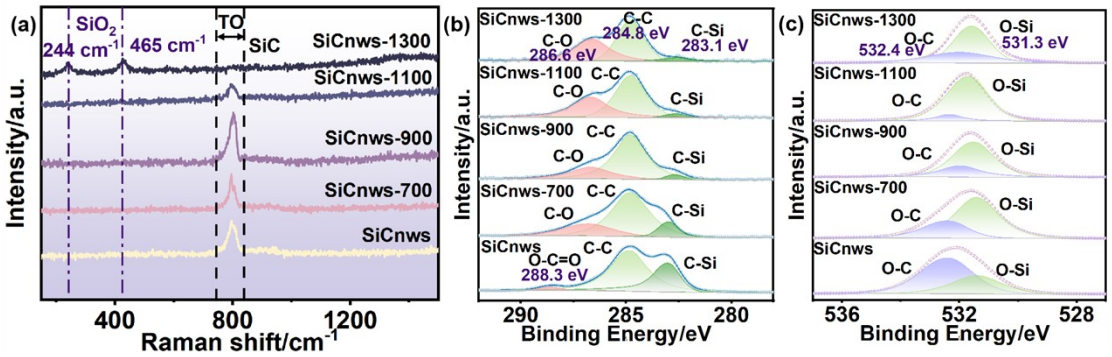

Fig. S7 Raman spectra of SiC aerogels at different oxidation temperatures (a); XPS fine spectra of C (b) and O (c) elements.

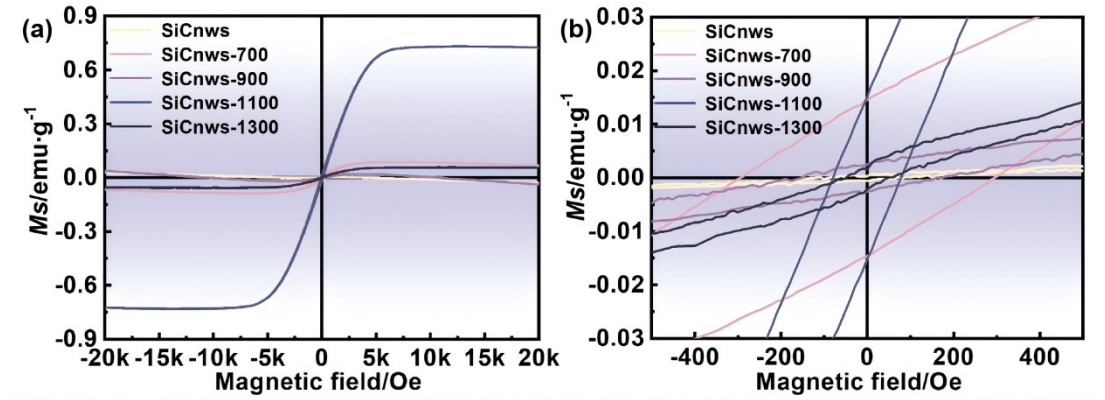

Fig. S8 Hysteresis loops image (a) and local magnifications (b) of SiC aerogels at different oxidation temperatures.

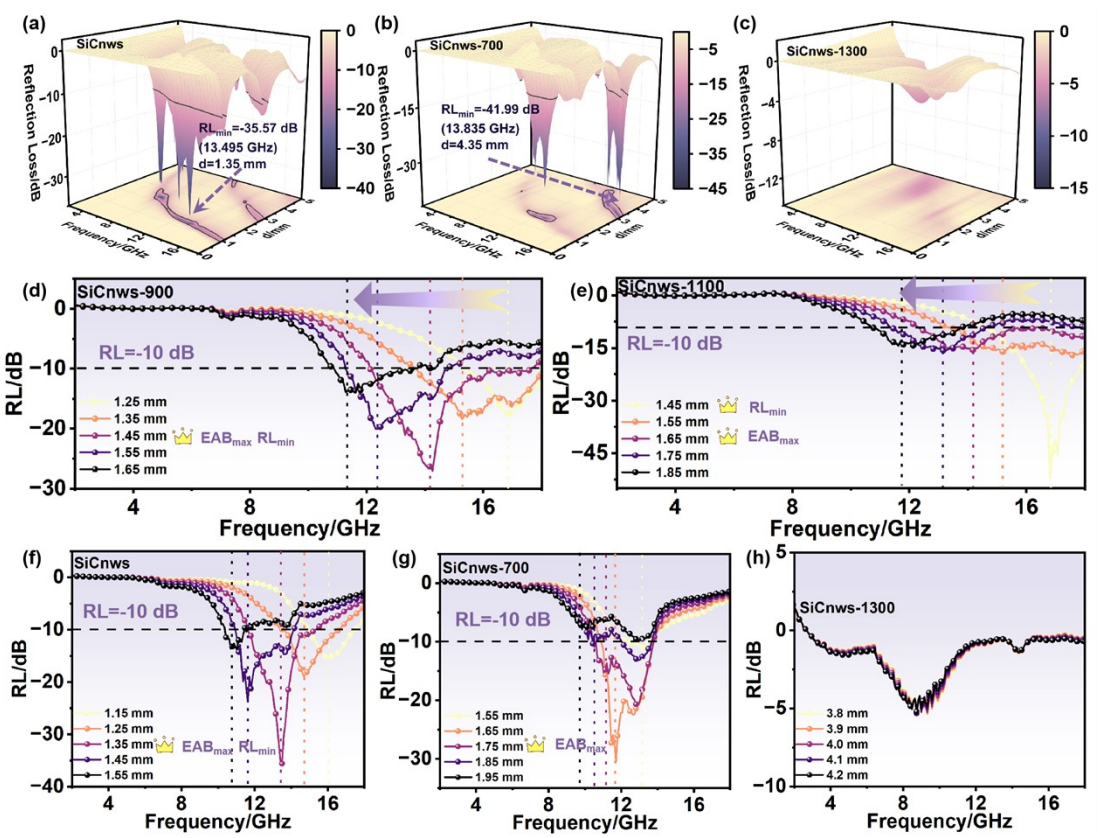

Fig. S9 3D reflection loss diagram of SiCnws (a), SiCnws-700 (b), SiCnws-1300 (c); and the change diagram of thickness of SiC aerogel with RL value at different oxidation temperatures (d-h).

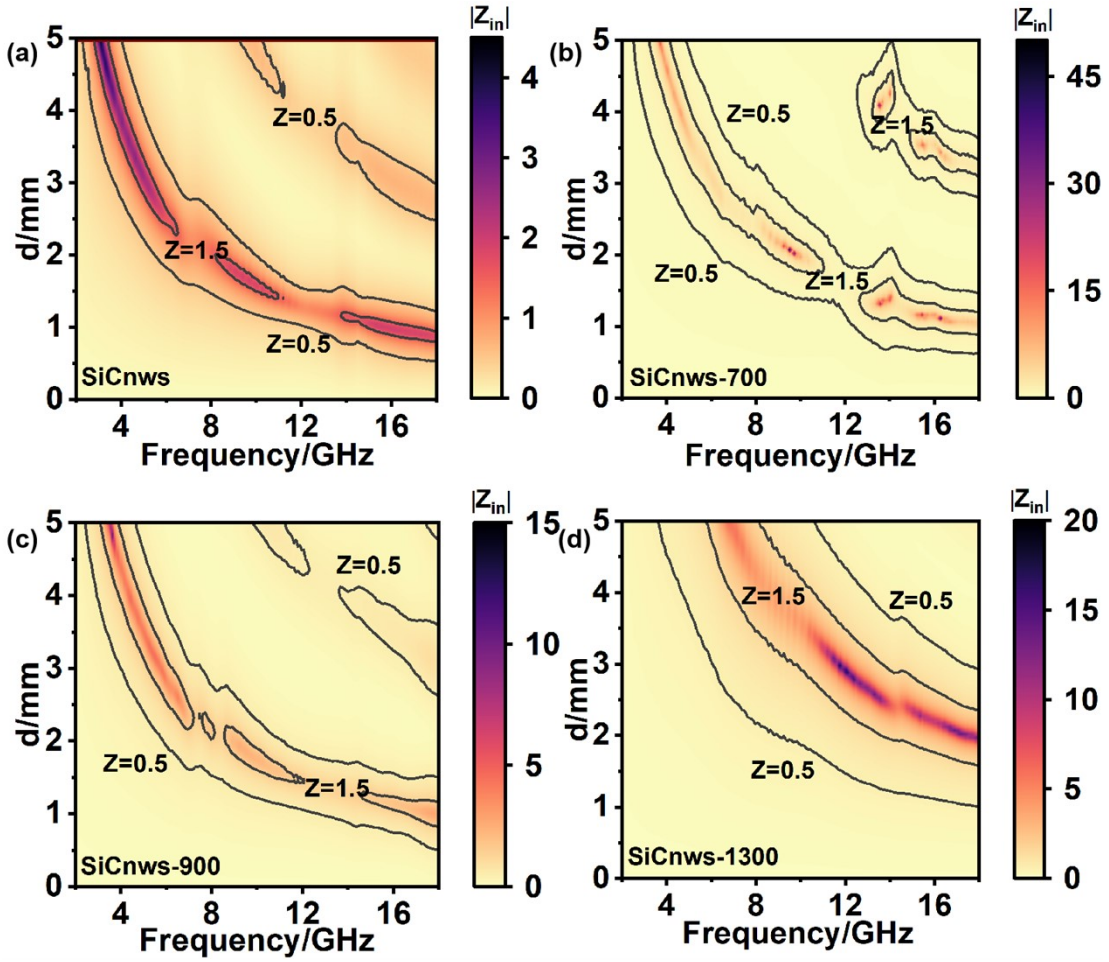

Fig. S10 Two dimensional impedance matching diagram of SiC aerogels at different oxidation temperatures.

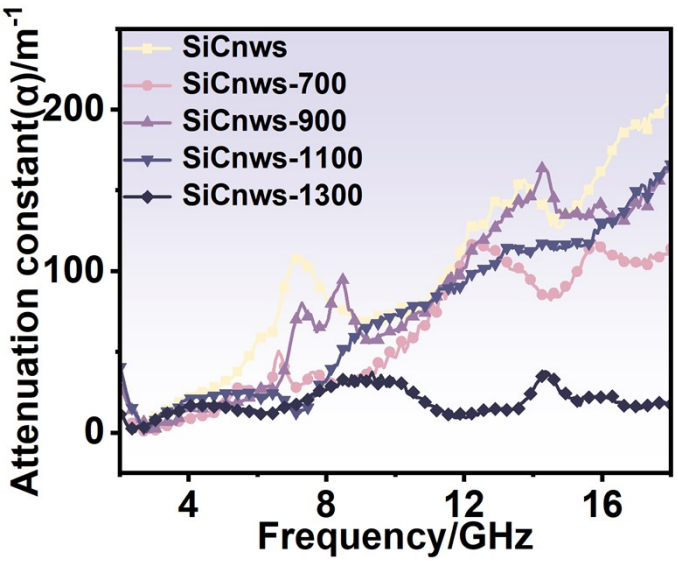

Fig. S11 Attenuation constants of SiC aerogels at different oxidation temperatures.

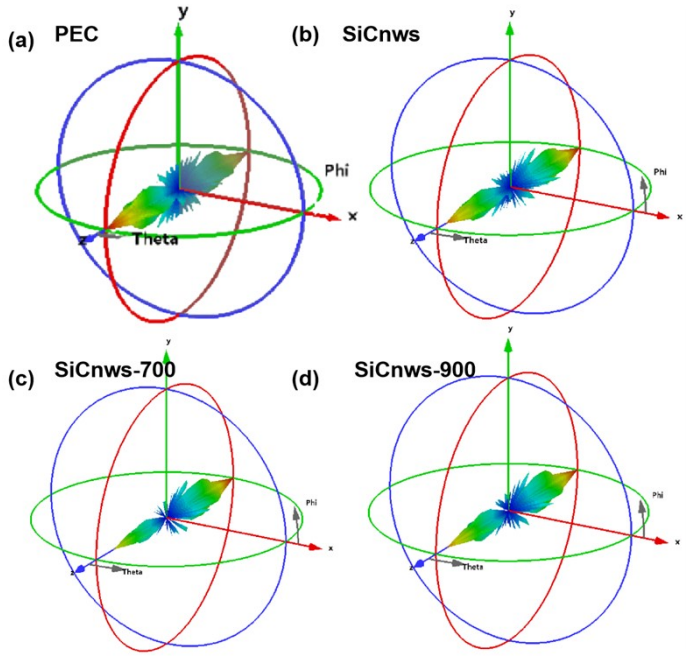

Fig. S12 RCS images of SiC aerogels at different oxidation temperatures.

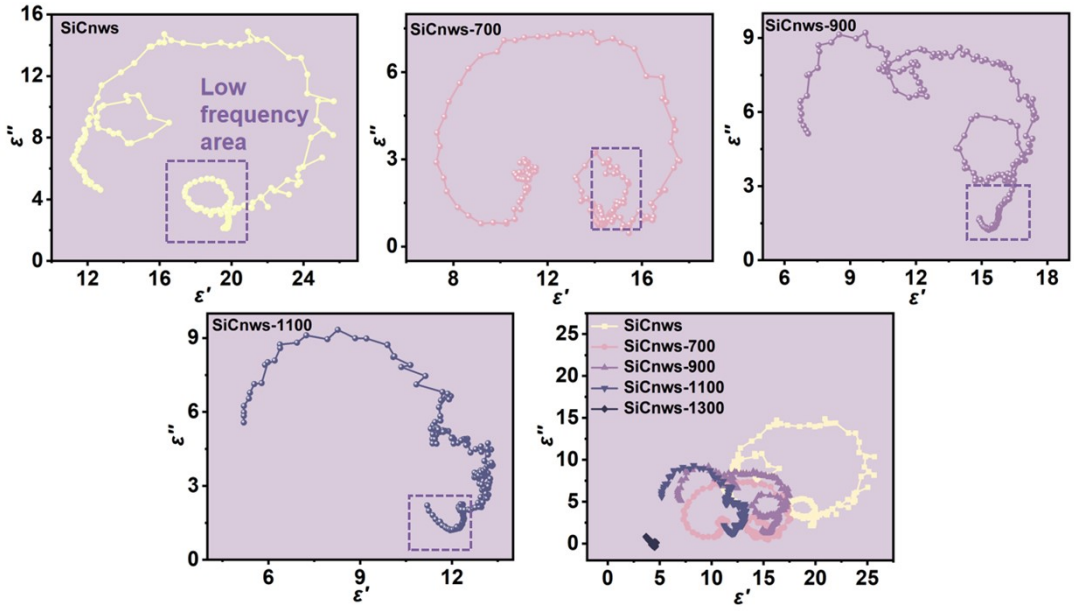

Fig. S 13 Cole-Cole plots of SiC aerogels at different oxidation temperatures.

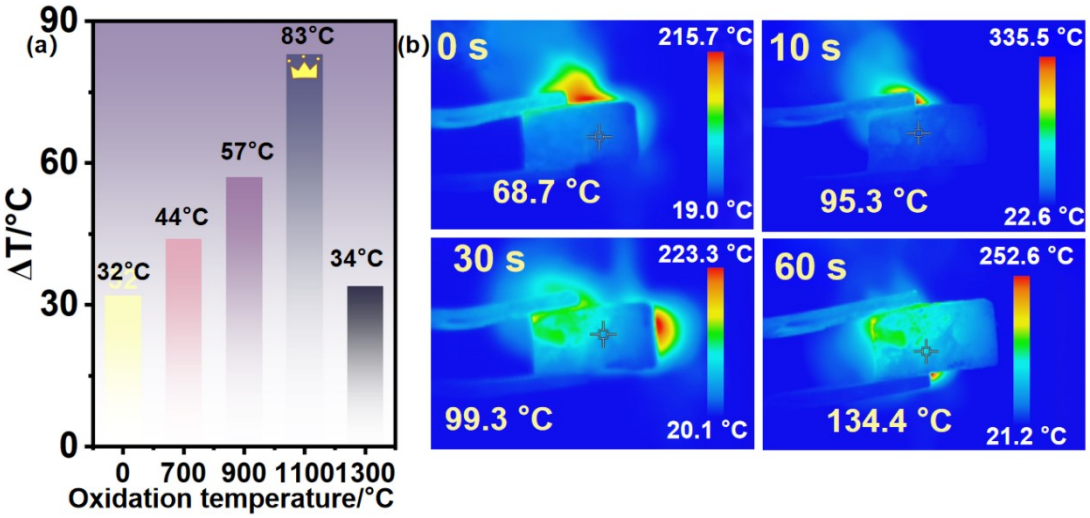

Fig. S 14 The difference of surface temperature of SiC aerogel under heating from the temperature of heating table (a); Thermal imaging photo of SiCnws-1100 backside under the action of high-temperature spray gun within 1 minute (b).

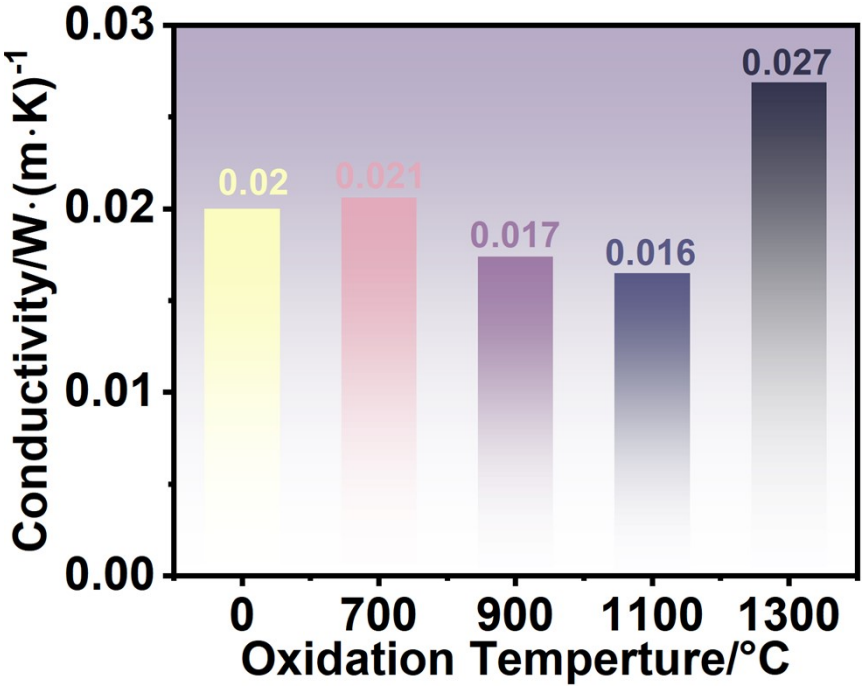

Fig. S15 Variation diagram of thermal conductivity of SiC aerogel

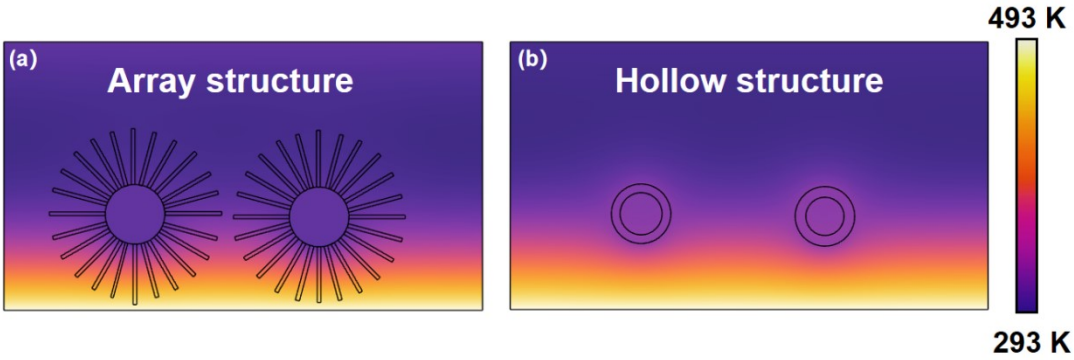

Fig. S 16 Thermal conductivity simulation images of individual array structures (a) or hollow structures (b).